International Journal of Plasticity 159 (2022) 103442

Contents lists available at ScienceDirect

International Journal of Plasticity

journal homepage: www.elsevier.com/locate/ijplas

On the deformation behavior of CoCrNi medium entropy alloys: Unraveling mechanistic competition

Ankit Gupta [a], Wu-Rong Jian [b], Shuozhi Xu [c], Irene J. Beyerlein [c,d], Garritt J. Tucker [a,*]

[a] Department of Mechanical Engineering, Colorado School of Mines, Golden, CO, USA
[b] Department of Mechanical Engineering, Stanford University, Stanford, CA 94305, USA
[c] Department of Mechanical Engineering, University of California, Santa Barbara, CA 93106-5070, USA
[d] Materials Department, University of California, Santa Barbara, CA 93106-5050, USA

A B S T R A C T

Recently, CoCrNi medium entropy alloys (MEA) have been the subject of numerous investigations due to their unique mechanical properties such as an exceptionally high strength-ductility combination. The resulting superior toughness of CoCrNi MEAs is attributed to an interplay of multiple deformation mechanisms, such as twinning, and partial and perfect dislocation glide. The current understanding of MEA deformation mostly stems from an indirect analysis of the defect evolution in deformed microstructures, where the contributions of individual mechanisms are assessed from the relative concentrations of associated defect structures. Here, we propose that the mechanistic contributions to microstructural deformation are more properly reflected by the percentages of total strain accommodation. Using atomistic simulations, the mechanical response of nanocrystalline CoCrNi MEA under uniaxial tension is investigated as function of grain size and chemical short-range ordering (SRO). The contributions of deformation mechanisms are resolved directly from the amount of strain accommodation by leveraging continuum based kinematic metrics. It is found that during initial loading, deformation occurs by partial dislocation slip, in agreement with experimental observations. Under continued loading, the governing deformation mechanisms transition to twinning and perfect dislocation slip. Furthermore, the grain size that corresponds to the maximum strength is found to decrease in presence of SRO.

1. Introduction

Equiatomic multi-component metallic alloys have recently attracted significant attention due to superior mechanical properties, such as outstanding radiation resistance and damage tolerance (El-Atwani et al., 2019; Inui et al., 2022). In the case of a ternary or a quaternary system, they are referred to as medium entropy alloys (MEA). One of the most widely investigated MEA system is the CoCrNi alloy, which is a subset of the CoCrFeMnNi (Cantor) alloy (Garcia Filho et al., 2022). CoCrNi MEA has a single-phase face centered cubic (FCC) structure with short-range chemical ordering that depends upon annealing temperature, and lattice distortions due to the presence of different atomic species (Zhang et al., 2020a). In several studies, the CoCrNi MEA is found to have both high strength and ductility and an exceptional fracture toughness, as compared to other alloys even at cryogenic temperature, making them an excellent candidate for applications that require high damage-tolerance (Gludovatz et al., 2016; Naeem et al., 2020; Zhang et al., 2017). The mechanical properties of CoCrNi MEAs can be further improved through microalloying (Feng et al., 2021; Zhang et al., 2021), nano-scale reinforcements (Wang et al., 2019a), non-equiatomic alloy compositions (Deng et al., 2021), or novel manufacturing methods (Han et al., 2021; Wang et al., 2019b).

Due to their unique set of properties, the relationship between the mechanical response of CoCrNi MEA and the underlying

* Corresponding author.
E-mail address: tucker@mines.edu (G.J. Tucker).

https://doi.org/10.1016/j.ijplas.2022.103442
Received 22 June 2022; Received in revised form 14 September 2022;
Available online 23 September 2022

deformation mechanisms have been the focus of many experimental studies that employ tensile and compressive testing (Ding et al., 2019; Gao et al., 2022; Laplanche et al., 2017; Li et al., 2022; Miao et al., 2017; Naeem et al., 2020; Praveen et al., 2018; Slone et al., 2018; Uzer et al., 2018; Zhao et al., 2017). Most of these studies reveal that deformation happens through partial dislocation slip in the early stages of loading followed by twinning. The exceptionally high strength-ductility combination of CoCrNi MEA is attributed to the synergy among multiple deformation mechanisms, such as twinning, and partial and perfect dislocation glide (Deng et al., 2019; Ding et al., 2019; Gludovatz et al., 2016; Laplanche et al., 2017).

It is proposed that the 3D twin network acts as a barrier to dislocation motion, leading to improvements in strength (Feng et al., 2020). Notably interconnected twin boundaries also offer several pathways for dislocation glide, which is suggested to simultaneously improve ductility by promoting a homogeneous distribution of plastic strain throughout the microstructure (Ding et al., 2019; Zhang et al., 2017). Thus, the formation of 3D twin networks is linked with an increase in the work hardening rate, which delays damage localization (Laplanche et al., 2017; Naeem et al., 2020; Zhang et al., 2020b). However, experimental evidence supporting this finding has largely included qualitative interpretations of defect evolution in microstructures during deformation. In some experimental studies, the underlying deformation mechanism is inferred from indirect quantitative measurements, such as change in work hardening rate (He et al., 2021; Laplanche et al., 2017; Li et al., 2022; Miao et al., 2017; Naeem et al., 2020; Uzer et al., 2018; Zhao et al., 2017), stacking fault probability or texture intensity (He et al., 2021; Naeem et al., 2020) as a function of the applied loading.

Simulations, capable of providing atomic scale insights, have been employed in several computational studies to elucidate the structure-property relationships in CoCrNi MEA and other derivatives of Cantor alloys (Ding et al., 2018a; Jian et al., 2021; Li et al., 2020a; Tian et al., 2020). Molecular dynamics (MD) simulations have been used in several works to elucidate the role of lattice distortion and local chemical ordering on the mechanical properties, such as hardness, yield strength, and ultimate strength (Jian et al., 2020; Li et al., 2020b; Yang et al., 2022). *Ab-initio* calculations have been employed to identify and even tailor the effect of chemical ordering on fault energies and the values of peaks or local minima in these energies have been used to gauge the relative contributions of deformation mechanisms (Ding et al., 2018b; Koch, 2017; Li et al., 2019; Zhang et al., 2020a). Other studies have quantified the role of individual deformation mechanism based upon number, length, area, or volume densities of different defect structures or types of dislocations during deformation (Hua et al., 2021; Jian et al., 2020; Wang et al., 2022; Xie et al., 2021). However, at the same time it has been argued that the contribution of a deformation mechanism to the overall deformation is best quantified by the amount of total strain it accommodates (Gupta et al., 2020a; Vo et al., 2008). Moreover, some mechanisms, such as perfect dislocation slip, do not leave behind defect traces that can properly reveal its deformation history.

Other factors, such as the high strain rates and the nanocrystalline (NC) grain sizes usually probed in MD simulations, make direct comparisons with experimental measurements, typically carried out at small strain rates and in coarse-grained materials, difficult. While inherent limitations remain, atomistic models and simulations, employing novel post-processing analysis, are uniquely situated to probe nanoscale mechanisms. In this study, the role of individual deformation mechanisms towards overall strain accommodation during uniaxial tensile deformation of NC CoCrNi MEA is quantified from atomistic simulations using continuum based kinematic metrics. The variation in the relative contributions of deformation mechanisms as a function of grain size and local chemical ordering is presented. The results are discussed in terms of planar fault energies and a twinnability parameter. Finally, the generalizations of these simulation results to grain sizes and strain rates typically probed in experiments are provided.

2. Method

2.1. Generation of NC structures

In this study, NC structures of pure Ni are generated from phase field simulations and converted to atomistic structures using the method outlined in (Gruber et al., 2017). These structures tend to be more realistic in terms of topologies of grains, grain boundaries (GBs), and triple junctions. Next, a two-step equilibration approach (Gupta et al., 2021) is employed, which significantly expedites the equilibration process, while still resulting in structural and mechanical properties that would be expected under thermal equilibration carried out at 300 K. The resulting set of NC structures have grain sizes ranging from 6 to 12 nm (~0.5 million to 4.3 million atoms), around 40 grains, randomly selected grain orientations, and 3D periodic boundaries. These pure Ni NC structures are then used as starting structures to create different equiatomic CoCrNi MEA configurations. The initial random elemental distribution for the CoCrNi MEA is constructed by randomly replacing 66.66% of Ni atoms with equal amounts of Cr and Co atoms.

To more broadly survey configurational space, the initial random MEA structures are subjected to hybrid Monte Carlo (MC) - Molecular Dynamics (MD) simulations under the variance constrained semi-grand canonical ensemble (Sadigh et al., 2012) at a temperature of 350 K, using the following chemical potential differences between Ni-Co $\mu_{NiCo} = 0.021$ eV and Ni-Cr $\mu_{NiCr} = -0.32$ eV. After every 1 MC cycle, 20 MD steps are performed in which the system is equilibrated in an NPT (isothermal-isobaric) ensemble at 350 K and zero normal pressure at the periodic boundaries. The MD time-step is 2.5 fs. In a previous study, it is found that the degree of short-range ordering (SRO) increases with decreasing annealing temperature and becomes constant below 650 K (Li et al., 2019). In the present study, a temperature of 350 K is chosen so that direct comparisons with previous modeling studies can be made in terms of the degree of SRO present near room temperature (Jian et al., 2020; Li et al., 2019). In every cycle, MC moves are performed on a quarter of the atoms. It is observed that after about 120,000 MC cycles, the system energy converges. The chemical SRO in the final MEA that results from the MC-MD simulations, is quantified using Warren-Cowley (WC) parameters (Cowley, 1950). The WC parameter α_{ij} between atomic species i and j, is defined as

$$\alpha_{ij} = \frac{f_{ij} - c_j}{\delta_{ij} - c_j} \tag{1}$$

where, f_{ij} is the number fraction of j-type atom in the 1st nearest neighbor shell of i-type atom, c_j is the concentration of j-type atom and δ_{ij} is the Kronecker delta function. Further details regarding the MC-MD simulation method and the WC parameters can be found in (Gupta et al., 2020b; Jian et al., 2020; Zhou et al., 2021). An embedded atom method potential is used to model the interatomic interactions in these simulations (Li et al., 2019). This potential has also been used and verified in previous studies by comparing lattice and elastic constants, cohesive energies and stacking fault energies to density field theory (DFT) calculations (Jian et al., 2020). All simulations are performed in LAMMPS (Plimpton, 1995) and visualizations carried in OVITO (Stukowski, 2010).

2.2. Mechanical testing

Mechanical behavior of the NC structures in uniaxial tension is simulated via MD. These simulations are performed at a constant strain rate and in an NPT ensemble at 1 K and zero normal pressure at the periodic surfaces in the transverse directions. Two strain rates of $10^8\ s^{-1}$ and $5 \times 10^8\ s^{-1}$ are selected for this study to probe strain-rate effects on deformation behavior. The MD time-step is 1 fs. To obtain the stress-strain behavior, the normal component of the resulting global stress tensor along the loading direction is plotted as a function of applied strain (i.e., fractional change in length of the simulation box in the loading direction). The slope of the stress-strain curve below 1% applied strain is used to obtain elastic stiffness. The yield stress and strain are calculated using the 0.2% offset method (Rajaram et al., 2020). The flow stress is the average of stress values in the flow regime (i.e., 6–16% applied strain).

2.3. Quantification of deformation mechanisms

The role of individual deformation mechanisms is resolved as a percentage of total strain accommodated in the loading direction at any point during uniaxial loading using microscale kinematic metrics (Tucker et al., 2016). For this purpose, the strain tensor of each atom is first calculated from the deformation gradient tensor by mapping the changes in the atomic positions of the nearest neighbors after deformation (Zimmerman et al., 2009). To calculate the total strain accommodated by individual deformation mechanisms, atoms are delineated into different groups corresponding to a given mechanism (i.e., twinning, dislocation slip, grain-elastic and GB deformation). The percentage of total loading strain p_j, accommodated by a deformation mechanism j, is given by Eq. (2).

$$p_j = \frac{\sum_{i=1}^{n_j} e_i^{kk} * 100}{\sum_{i=1}^{N} e_i^{kk}} \tag{2}$$

Here, e_i^{kk} is the normal component of the strain tensor of atom i, in the loading direction, k. The summation in the numerator spans over all atoms n_j, associated with mechanism j, while the denominator denotes the summation of strain tensor components over the total number of atoms N, in the NC structure. The fraction of total atoms f_j, participating in mechanism j, can then be defined as $\frac{n_j}{N}$.

The classification of atoms into different deformation mechanisms is based on certain kinematic signatures, such as slip vector, microrotation, von Mises strain, and structural environment (FCC/Hexagonal Close Packed/Other) of each atom (Tucker et al., 2016). Accordingly, FCC atoms that have a computed slip vector and von Mises strain matching that of perfect dislocation slip, are classified into the perfect dislocation group. Similarly, the partial dislocation group contains atoms within stacking faults that have a calculated slip vector and von Mises strain associated with the Burgers vector of partial dislocation slip. The twinning group includes atoms belonging to twin boundaries and twinned regions. Twinned regions are comprised of FCC coordinated atoms with an additional kinematic signature of being traversed by a migrating twin boundary (Gupta et al., 2020a; Tucker and Foiles, 2015). Remaining FCC atoms that do not belong to either the dislocation or twinning group, deformed in an elastic manner, and are classified into the grain-elastic group. The GB deformation group contains GB atoms that deform either in an elastic manner (i.e., reversible deformation) (Gupta et al., 2020a; Rajaram et al., 2020) or by plastic mechanisms, such as GB sliding, migration, and restructuring through atomic shuffling or shear events. More details regarding the quantification of deformation mechanisms can be found in (Gupta et al., 2020a).

2.4. Estimation of fault energies

The generalized planar fault energy (GPFE) curves are obtained by first creating a single crystalline block for the FCC system of interest, with <110>, <112>, and <111> crystallographic directions aligned along the x, y, and z axis of the simulation box, respectively. The simulation box has 30, 90, and 120 repeating unit cells along the x, y, and z directions, respectively, and around 200,000 atoms. Periodic boundary conditions are applied only along the x and y directions. The GPFE curves are obtained from displacing the top half of the simulation box in increments of 0.01 Å along the (111) plane in the <112> directions until a stacking fault is created. After each increment, the resulting configuration is relaxed using constrained energy minimization, i.e., the system is allowed to relax only along the z direction (Li et al., 2019). Samples with stacking faults are used as starting configurations for calculating subsequent twinning fault energy curves. To ensure a good statistical representation, 40 different configurations are created for CoCrNi samples, both with and without SRO. The calculated GPFE curve for each sample is thus an average of 120 curves (40 configurations each of the three different <112> in-plane slip directions).

3. Results

3.1. Structure and mechanical response of NC MEA

Fig. 1a and 1b show the initial and final structures (i.e., before and after MC-MD simulations) of equiatomic NC CoCrNi MEA, respectively, with an average grain size of 12 nm. In the initial structure, there is no SRO. A random distribution of Ni, Co and Cr atoms is present, as can be seen in the inset. In the final structure (Fig. 1b), obtained after hybrid MC-MD simulations, some degree of chemical SRO is observed, in agreement with experimental findings (Zhang et al., 2020a; Zhou et al., 2022). It should be noted here that the presence of SRO is quantitatively established in the experimental studies from the extra diffuse spots observed in diffraction and Fast Fourier transform patterns under transmission electron microscopy. From these patterns, the nature of SRO is qualitatively suggested to be such that Cr-Cr pairs between the nearest neighbors are strongly suppressed (Zhang et al., 2020a). In a more recent study, quantitative atomic-resolution energy dispersive spectroscopy mapping indicated a tendency for avoidance of like-pairs and preference for unlike-pairs between the nearest neighbors (Zhou et al., 2022).

In the current study, preferential bonding between Co and Cr atoms and between like Ni atoms can be seen in the structure with SRO (inset to Fig. 1b). The local ordering present in the final structure is quantified in Fig. 1c in terms of the average WC parameters between the atomic pairs. The WC parameters for the CoCr and NiNi pairs are large negative and positive values, respectively, indicating some degree of clustering between these unlike and like species pairs. On the other hand, the WC parameters for the Ni-Co and Ni-Cr pairs are large positive values, indicating a tendency of avoidance of these unlike-pairs. The WC values for the CoCo and CrCr pairs are small, which suggests a lack of SRO for those elemental pairs. These trends are consistent with those from previous atomistic simulations on CoCrNi MEA (Jian et al., 2020; Yang et al., 2022).

Table 1 provides the composition of different atomic species in GB and intragranular (IG) regions in the MEA structure with SRO. We find that Co and Cr atoms are more segregated towards GBs and Ni atoms are more segregated in IG regions. Fig. 1d shows the stress-strain curves obtained from the uniaxial tensile loading of the NC CoCrNi MEA structures of 12 nm grain size at a strain rate of 10^8 s^{-1}. The results for structures with and without SRO are compared. The MEA structure with a random distribution of different atomic species (i.e., without SRO) has a lower elastic stiffness, yield strain, yield stress, and flow stress than the structure with SRO (Table 2). Similar effects of chemical ordering on the mechanical properties of CoCrNi MEA have also been reported previously (Jian et al., 2020).

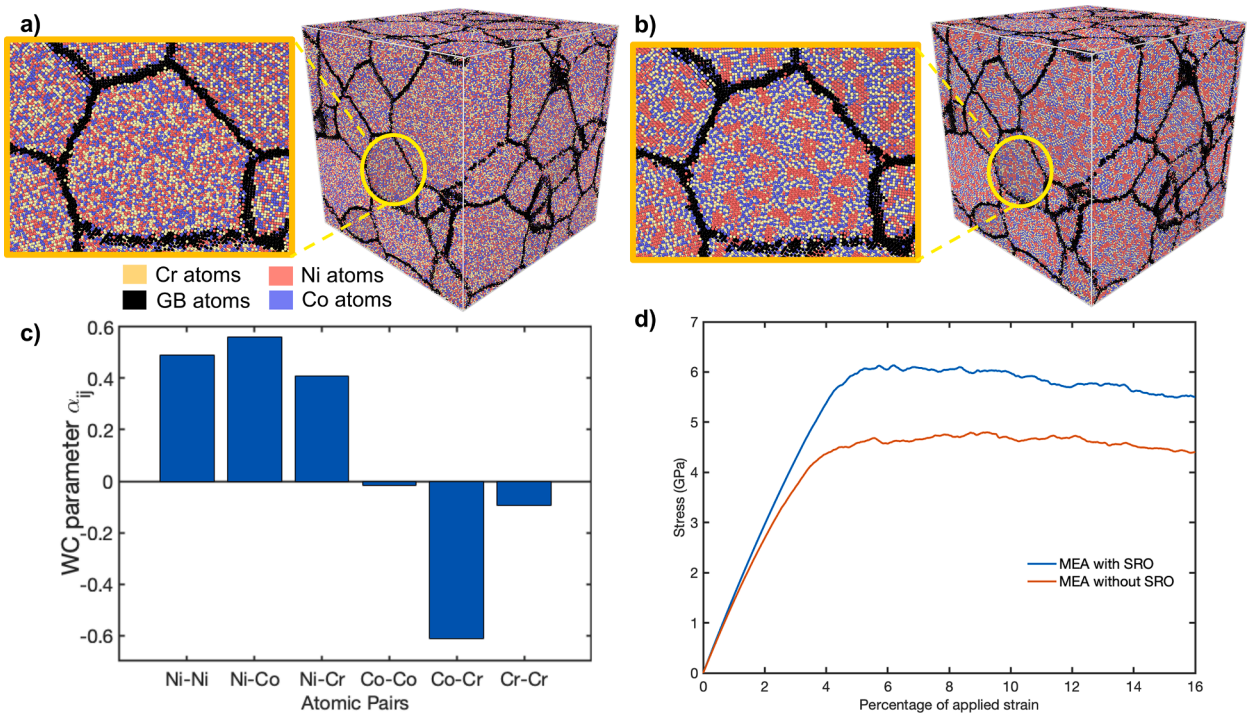

Fig. 1. 12 nm grain size NC CoCrNi MEA structures (**a**) without and (**b**) with SRO (insets to the figures show a small region with corresponding distribution of different atomic species). (**c**) A bar plot of the average Warren-Cowley parameters, α_{ij}, for different atomic species pairs in the final NC structure, obtained after hybrid MC-MD simulations. (**d**) Stress-strain curves of the 12 nm grain size NC MEA structures with and without SRO as obtained from the uniaxial tension MD simulations at a strain rate of 10^8 s^{-1} (plotted values are the averages obtained from loading along the three orthogonal directions).

Table 1
Composition of different atomic species in the grain boundary (GB) and intragranular (IG) regions of the 12 nm grain size NC CoCrNi MEA structure with SRO.

Region	Ni (%)	Co (%)	Cr (%)
Grain Boundary (GB)	28.3	36.2	35.4
Intragranular (IG)	34.8	32.5	32.7

Table 2
Mechanical properties of the 12 nm grain size NC CoCrNi MEA structures with and without SRO as obtained from the uniaxial tension stress-strain curves (values are the averages obtained from loading along the three orthogonal directions along with their standard deviations).

MEA configuration	Elastic Stiffness (GPa)	Yield Strain (%)	Yield Stress (GPa)	Flow Stress (GPa)
With SRO	155.4 ± 9.0	2.69 ± 0.04	3.86 ± 0.28	5.84 ± 0.09
Without SRO	145.6 ± 7.8	2.21 ± 0.03	2.90 ± 0.19	4.63 ± 0.06

3.2. Deformation mechanisms in NC MEA

The percentages of total strain accommodated by different deformation mechanisms p_j, during the uniaxial tensile loading of the two MEA structures are shown in Fig. 2a. In both structures (i.e., with and without SRO), the total tensile strain is accommodated between the GBs and the elastic deformation of grains during the early stage of loading (i.e., before yield). By delineating the elastic and the plastic components, it was previously shown that most of the strain accommodated by GBs during this initial loading is also elastic in nature and vanishes upon unloading (Gupta et al., 2020a; Rajaram et al., 2020). On continued loading, the amount of plastic strain accumulated in the GBs due to micro-yielding events (Gupta et al., 2020a; Rajaram et al., 2020), and hence the total GB strain increases while the elastic strain in the grains decreases, as can be seen in Fig. 2a. At some critical value of applied strain, the contribution of dislocation mechanisms towards strain accommodation also starts to rise. This value is larger for the MEA structure with SRO. With further increases in load, twinning begins to accommodate strain.

The average contribution of different mechanisms during the flow regime $\overline{p_j}$, in terms of percentage of total strain accommodation (i.e., p_j averaged over 6-16% applied strain), is shown in Table 3. GB mechanisms (e.g., sliding, atomic shuffling, etc.) are observed to accommodate a significant amount of microstructural strain during the flow regime. However, all the IG mechanisms combined accommodate the largest amount of strain (i.e., greater than 50%) and therefore, govern the deformation response at this grain size (i.e., 12 nm), regardless of the degree of SRO. The contribution of dislocation slip is the highest amongst the IG mechanisms. The contribution of twinning is relatively small, and the remaining IG strain is accommodated by elastic deformation of grains and defect structures formed inside the grains due to the intersection of dislocations and twins gliding on different planes (i.e., the "other" group/mechanism in Fig. 2a). These mechanisms are illustrated in Fig. 3. It should be noted here that we don't observe large amorphous regions in these deformed MEA structures unlike experimental microstructures subjected to extreme deformation (Ming et al., 2020; Zhao et al., 2021) or atomistic structures tested under quasi-isentropic compression or shock loading (Jian et al., 2022; Xie et al., 2022).

Table 3 shows that the grain-elastic contribution to overall deformation is comparatively large, even in the flow regime. In NC

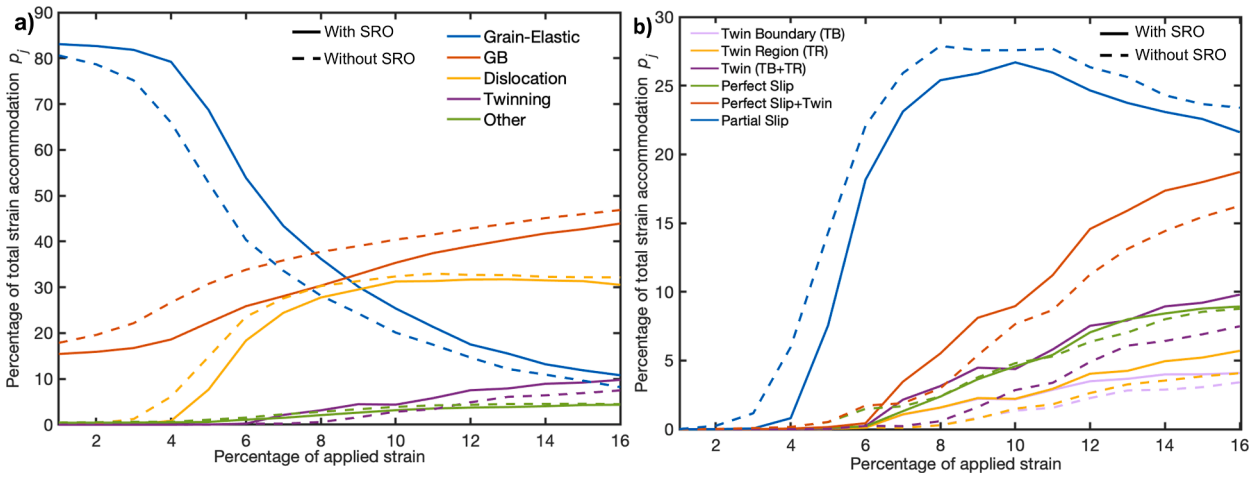

Fig. 2. Percentages of total strain accommodation p_j, by **(a)** individual deformation mechanisms and **(b)** delineated IG mechanisms, as a function of applied strain, during the uniaxial tensile loading of the 12 nm grain size NC CoCrNi MEA structures with (solid lines) and without (dashed lines) SRO.

Table 3
Average percentages of total strain accommodation by individual deformation mechanisms $\overline{p_j}$, during the flow regime of the uniaxial tensile loading of the 12 nm grain size MEA structures with and without SRO.

MEA configuration	Grain-Elastic	Dislocation	Twinning	Other	IG	GB
With SRO	25.39	29.05	5.78	3.12	63.34	36.15
Without SRO	19.97	30.92	3.70	3.69	58.28	41.19

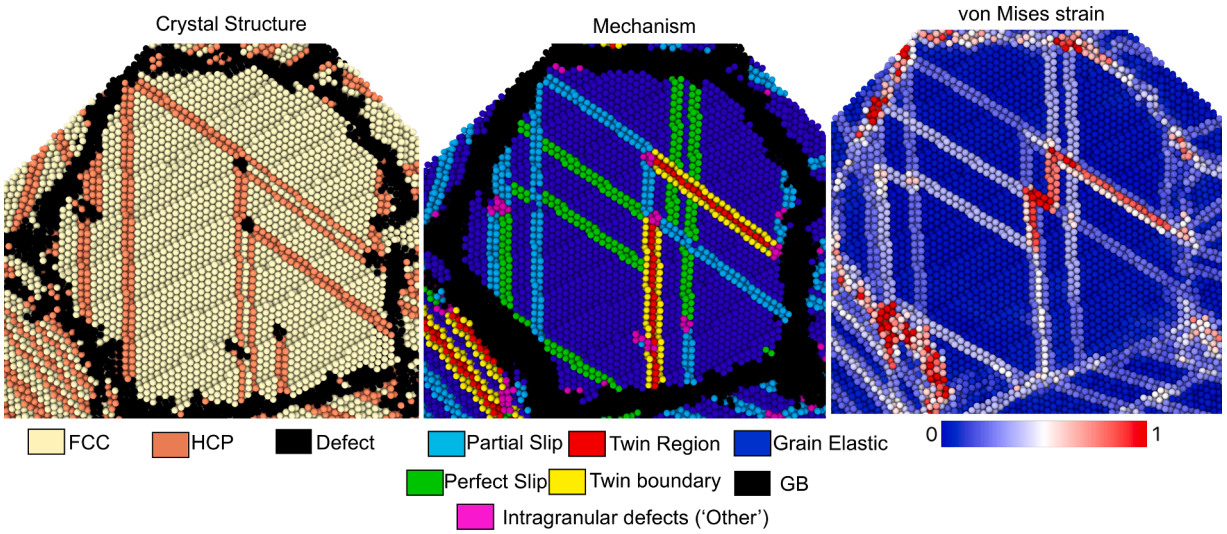

Fig. 3. Slices through deformed NC MEA structure of 12 nm grain size with SRO, at 16% applied strain. Atoms in slices are colored according to crystal structure, deformation mechanisms, and von Mises strain.

metals, the grain-elastic contribution to total strain is expected to be higher than that of their coarser-grained counterparts. The large degree of elastic strain is a consequence of the higher stresses necessary to induce plastic deformation in NC metals (Gupta et al., 2020a). The grain-elastic contribution decreases during the later stages of flow as the contribution of GB mechanisms and additional IG mechanisms such as twinning increases (Fig. 2a). In the flow regime (Table 3), the average contributions of GB mechanisms and dislocation slip are slightly higher in the MEA structure without SRO, while twinning is more pronounced in the MEA structure with SRO.

Fig. 2b further delineates the resolved contributions towards strain accommodation of dislocation and twinning in the two MEA structures. Partial slip starts accommodating strain around 3% and 2% applied strain in MEA structures with and without SRO, respectively. The contribution of partial slip peaks around 10% applied strain and tends to decrease afterwards in both structures. On the other hand, the contribution of perfect dislocation slip rises around 6% and 5% applied strain, respectively, in MEA structures with and without SRO, and increases monotonically with continued straining. The percentage strain accommodated by twinning increases around same time as perfect dislocation slip, i.e., at 6% applied strain in the MEA with SRO. Twinning activates after perfect dislocation slip, at around 8% applied strain in the MEA without SRO.

Twinning and perfect dislocation slip exhibit similar strain accommodation in the MEA structure with SRO, but twinning accommodates less strain than perfect slip in the MEA structure without SRO (Fig. 2b). In both structures, the contributions of twin boundaries relative to twinned regions (i.e., between two twin boundaries) are similar. Furthermore, while partial dislocation slip accommodates the highest amount of strain, its contribution becomes comparable to the total contribution of perfect dislocation slip and twinning at large values of applied strain. The trends seen in Fig. 2b suggest that perfect slip and twinning together should overtake partial slip as the dominant IG mechanism when the uniaxial strain is increased beyond 16%. However, this mechanistic cross-over would take place at a smaller value of the applied strain in the MEA structure with SRO because the local chemical ordering makes twinning more pronounced, and as shown in Fig. 2b, the contribution of partial slip towards strain accommodation decreases as compared to the MEA structure without SRO. It should be note here that the trend observed in Fig. 2b is confirmed by continuing the loading of MEA structure with SRO till 24% strain. It is found that the combined contribution of perfect slip and twinning surpasses partial slip at around 19% applied strain and the contribution of twinning relative to perfect slip becomes higher on continued loading (Supplementary Fig. 1).

3.3. *Effect of grain size*

The variation in average contributions of deformation mechanisms during the flow regime $\overline{p_j}$, as a function of grain size, is pre-

sented in Fig. 4a, for MEA structures with and without SRO. For this grain size effect study, the tensile testing simulations were performed at a strain rate of 5×10^8 s^{-1}, in order to reduce the total simulation time. The trends in the variation of SRO for atomic species pairs are similar across different grain sizes as shown in Fig. 4b, experiencing only a slight increase in the magnitudes as grain size decreases from 12 nm to 6 nm. The flow stress, however, is more sensitive to grain size.

The flow stress of structures with SRO initially increases on decreasing the grain size below 12 nm, peaks around a grain size of 8 nm, and then decreases with further reductions in grain size (Fig. 4c). 8 nm is found to be the strongest grain size in NC MEA with SRO; smaller than the value reported for NC Ni (Gupta et al., 2020a). The flow stress of NC structures without SRO is smaller than the ones with SRO across all grain sizes (Fig. 4c), but the trends in their variation are similar. The strongest grain size in NC MEA without SRO is found to be 10 nm, larger than that of NC MEA with SRO. This variation would suggest a change in the dominant mechanism with grain size (Gupta et al., 2020a; Spearot et al., 2019).

Fig. 4a shows that as the grain size decreases, the contribution from GB mechanisms (e.g., sliding, atomic shuffling, etc.) increases while that of IG mechanisms (mainly dislocation slip) decreases in both MEA structures, i.e., with and without SRO. Below a grain size of 8 nm, GB mechanisms become the dominant deformation mechanism in MEA structures with SRO, since it accommodates the most amount of strain. As compared to MEA structures with SRO, the contribution of GB mechanisms is higher in MEA structures without SRO across all grain sizes. Reverse is true for the contribution of IG mechanisms. Therefore, GB mechanisms become the dominant deformation mechanism at a larger grain size in MEA structures without SRO.

The grain size at which the mechanistic cross-over between the GB and the IG mechanisms occurs (Fig. 4a), also corresponds to the maximum strength, calculated in terms of flow stress (Fig. 4c) for both MEA structures. This is an important finding. It verifies the previously proposed notion that the maximum strength of polycrystalline materials corresponds to the grain size regime, where the dominant deformation mechanism changes (Spearot et al., 2019). However, in agreement with a more recent study (Gupta et al., 2020a), it is found that the mechanistic transition at maximum strength is between GB mechanisms and all IG mechanisms combined and not just twinning or dislocation slip, as presumed earlier (Spearot et al., 2019).

4. Discussion

4.1. Nucleation of leading partials

The aforementioned deformation behavior of MEA alloys is now considered on the basis of the energies of different planar faults in FCC materials, calculated from the GPFE curves in Fig. 5a. The results for pure Ni are also included for comparison. The contributions of IG mechanisms during the uniaxial tensile loading of NC Ni, as a function of the applied strain, are shown in Fig. 5b. Table 4 provides some quantities of interest from the GPFE curves. The first one is the energy barrier associated with the nucleation of the leading partial dislocation, i.e., the unstable stacking fault energy (γ_{us}). A higher value of γ_{us} suggests that a larger stress will be required to nucleate a leading partial (Rice, 1992; Van Swygenhoven et al., 2004). This explains the higher yield strength of the NC MEA structure with SRO,

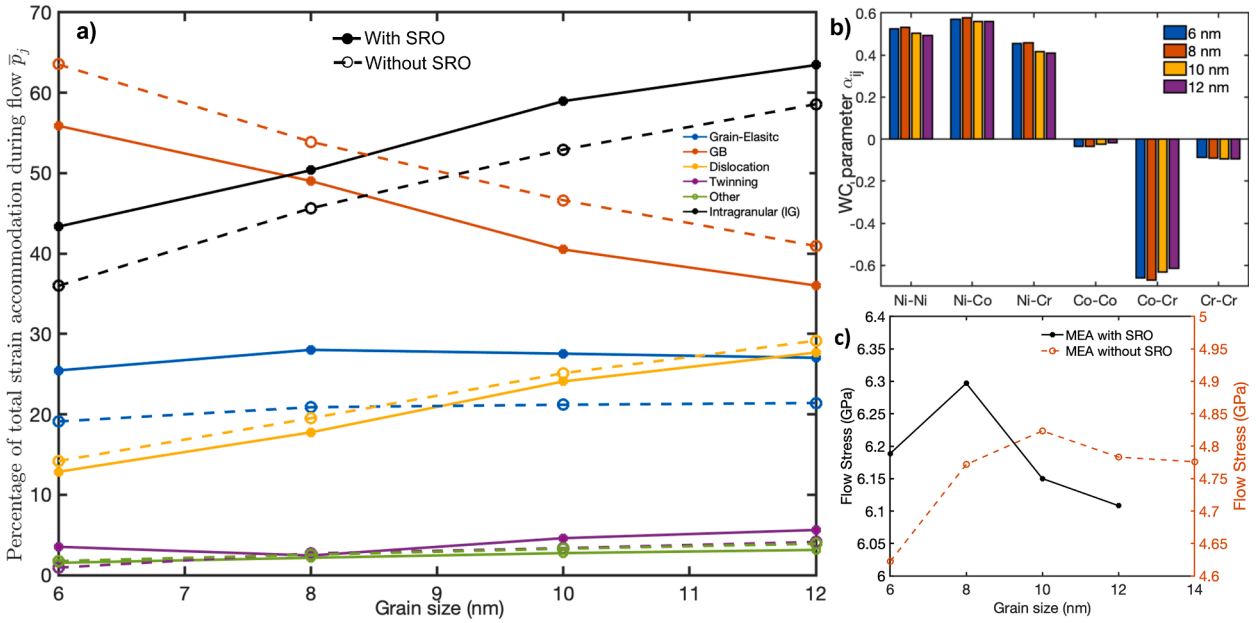

Fig. 4. **(a)** Average percentages of total strain accommodation by individual deformation mechanisms during the flow regime $\overline{p_j}$, as a function of grain size of the NC MEA structures with (solid lines) and without (dashed lines) SRO, obtained from the uniaxial tensile loading at a strain rate of 5×10^8 s^{-1}. **(b)** Bar plots of the average WC parameters α_{ij}, in the NC MEA structures with SRO of different grain sizes. **(c)** Variation of flow stress as a function of grain size in the NC MEA structures with (solid lines) and without (dashed lines) SRO.

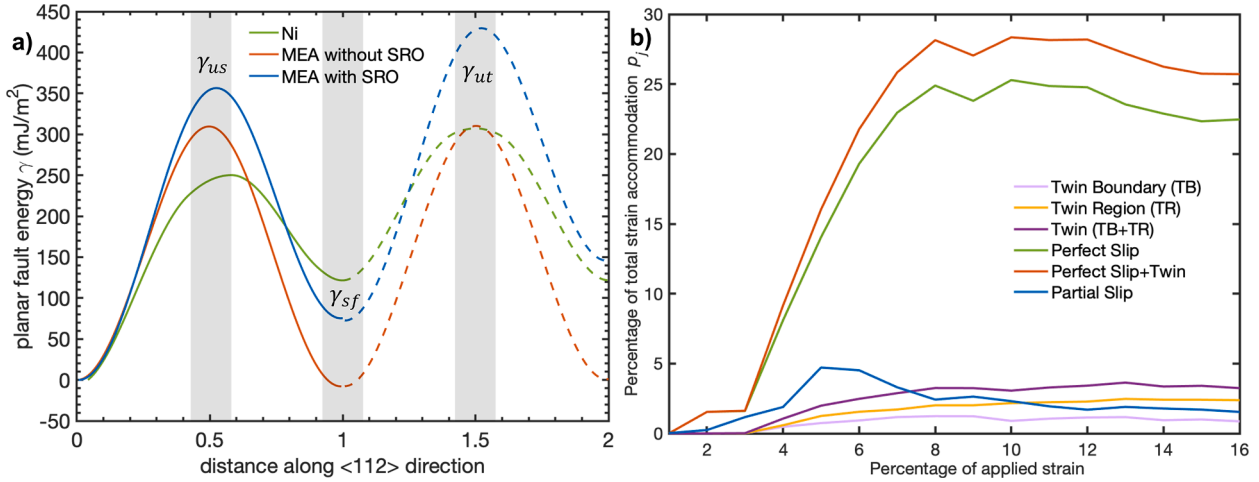

Fig. 5. **(a)** GPFE curves for the stacking (solid lines) and twin (dashed lines) fault planar defects in MEA CoCrNi, with and without SRO, and Ni. The unit length along <112> direction is equal to the Burgers vector of partial slip. **(b)** Percentages of total strain accommodation by IG mechanisms p_j, as a function of applied strain, during the uniaxial tensile loading of NC Ni structure of 12 nm grain size at 10^8 s^{-1} strain rate.

Table 4
Energies and parameters of interest, calculated from the GPFE curves of MEA CoCrNi, with and without SRO, and Ni (energies for MEA are the averages obtained from 120 curves along with their standard deviations).

FCC systems	γ_{us} (mJ/m^2)	γ_{sf} (mJ/m^2)	γ_{ut} (mJ/m^2)	$\frac{\gamma_{sf}}{\gamma_{us}}$	ζ
MEA with SRO	355.5 ± 5.3	73.1 ± 8.6	429.5 ± 6.9	0.20	1.01
MEA without SRO	309.6 ± 4.5	-7.7 ± 3.9	310.2 ± 5.9	0.02	1.14
Ni	250.1	121.6	307.1	0.49	0.96

as it is found that γ_{us} increases with SRO, in agreement with previous studies (Jian et al., 2020; Li et al., 2019; Yang et al., 2022).

As shown in Fig. 6, the emission and propagation of a leading partial from the GBs occur at a larger value of applied strain in the MEA structure with SRO than the one without. A trend also reflected in Fig. 2b, where the contribution of partial dislocation slip is seen to rise at a larger value of applied strain in the MEA structure with SRO. In both structures (Fig. 6a and b), however, partial dislocations emit from the GB regions with von Mises strain above a critical value, indicative of some minimum GB deformation associated with the nucleation of a partial dislocation. This suggests that deformation occurs by stress-assisted free volume migration and atomic shuffling

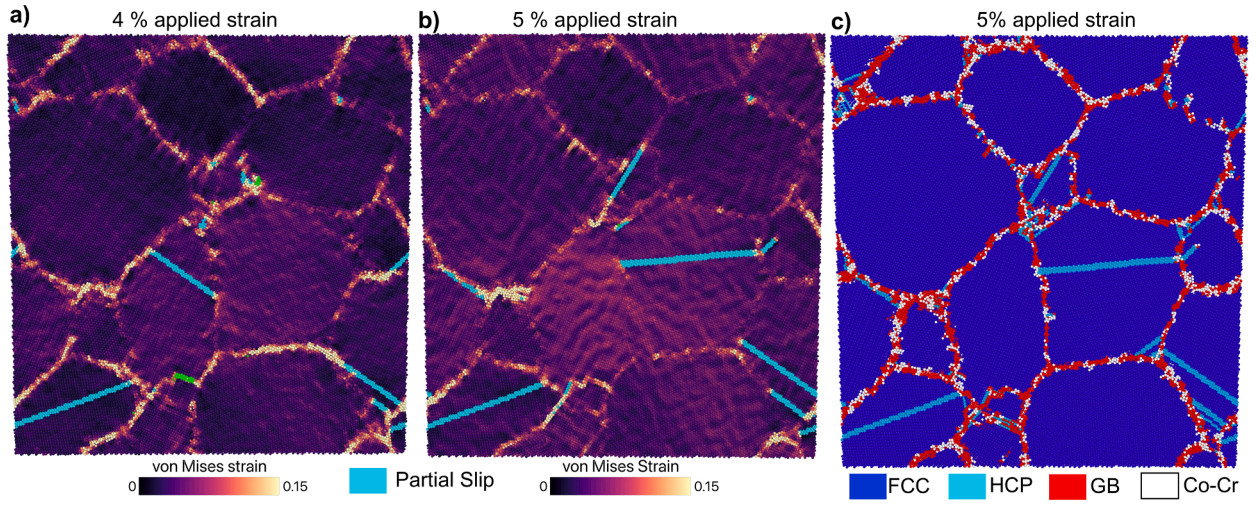

Fig. 6. Slices through NC MEA structures of 12 nm grain size **(a)** without and **(b), (c)** with SRO, deformed under uniaxial tension at a strain rate of 10^8 s^{-1}. Atoms in the slices are colored according to **(a), (b)** von mises strain and **(c)** crystal structure (Co, Cr atoms at the GBs with magnitude of WC parameters greater than 0.58, are also highlighted in white).

events in the GBs (Van Swygenhoven et al., 2002).

In the MEA structure with SRO, the partials can be seen emitting from the CoCr clusters in the GBs with larger degree of chemical ordering (Fig. 6c), which also maps to regions of high von Mises strain shown in Fig. 6b. In a previous computational study (Jian et al., 2020), CoCr clusters were suggested to be the preferential nucleation site due to their smaller γ_{us}, compared to pure Ni. However, the contribution of the GB mechanisms towards overall strain accommodation during the uniaxial loading of MEA structures, is found to be higher when Co, Cr and Ni atoms were distributed randomly (Fig. 2a). Therefore, these results suggest that the presence of local chemical order should strengthen the GBs, as also reported in experiments (Schuh et al., 2018).

4.2. Competition between partial and perfect dislocation slip

Once the leading partial is emitted from the GB, the energy barrier for the nucleation of the trailing partial dislocation is proportional to $\gamma_{us} - \gamma_{sf}$ (Rice, 1992), where, γ_{sf} is the stacking fault energy. Using MD simulations, it is previously shown that the ratio, $\frac{\gamma_{sf}}{\gamma_{us}}$, dictates the nature of dislocation activity (i.e., perfect versus partial slip) in several NC materials (Van Swygenhoven et al., 2004). In the current study, this ratio is calculated to be small (i.e., < 0.2) for both MEA configurations (Table 4). On the contrary, the $\frac{\gamma_{sf}}{\gamma_{us}}$ ratio is higher in NC Ni (Table 4), where perfect dislocation slip is found to be the dominant IG deformation mechanism during uniaxial tensile loading (Fig. 5b), another result in tandem with the findings of experimental studies that reported no increase in either stacking fault or twin density during tensile deformation of NC Ni (Frøseth et al., 2004).

The higher $\frac{\gamma_{sf}}{\gamma_{us}}$ ratio found in case of pure Ni, represents a smaller energy barrier for the nucleation of the trailing partial at the GBs,

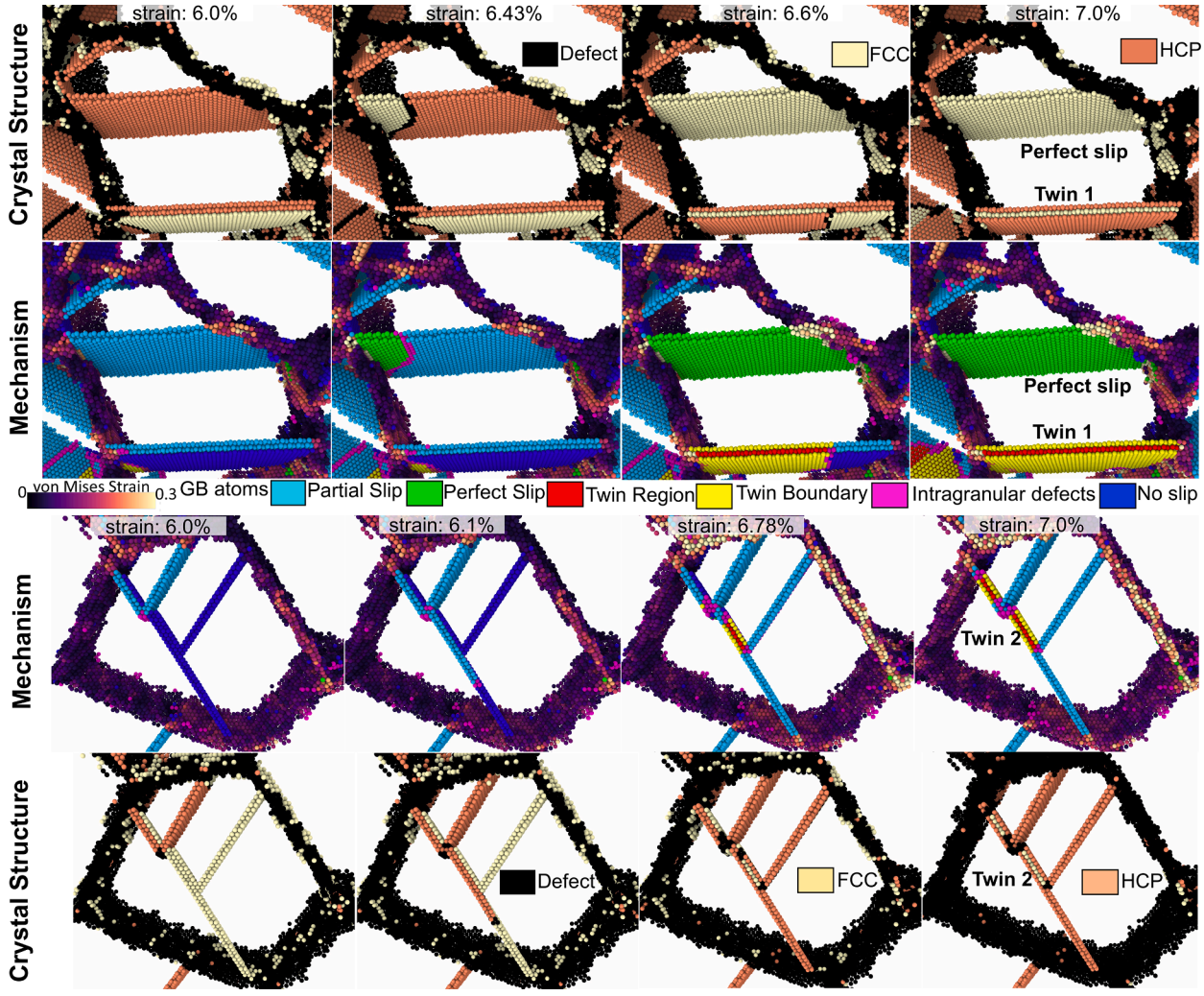

Fig. 7. Slices through deformed NC MEA structure of 12 nm grain size with SRO, at different percentages of applied strain (elastically deformed atoms are not shown). Atoms in the slices are colored according to crystal structure and deformation mechanisms (atoms in GB mechanisms are colored according to von Mises strain).

which allows for the observation of perfect dislocation even at lower applied strains. However, in the case of NC MEA structures with smaller values of $\frac{\gamma_{sf}}{\gamma_{us}}$, the energy barriers for nucleating the trailing partial are higher. Therefore, partial dislocation slip is observed to be the dominant IG mechanism in MEA structures and perfect dislocation slip that requires nucleation of a trailing partial, tends to accommodate strain only during later stages of deformation (Fig. 2b). Within the two MEA structures, the $\frac{\gamma_{sf}}{\gamma_{us}}$ ratio is smaller for the structure without SRO, which explains its larger contribution of partial slip as compared to the structure with SRO (Fig. 2b).

4.3. Competition between perfect dislocation slip and twinning

Perfect dislocation slip in the NC MEA occurs through the nucleation of a trailing partial at the GB and its glide on the same slip plane as the leading partial, as shown in Fig. 7. Two different twinning mechanisms (Jian et al., 2020) are observed during deformation of NC MEA (Fig. 7). The first mechanism (*Twin 1*) involves nucleation of a second leading partial at the GB and its glide on a slip plane adjacent to the first leading partial, thus making GBs the twinning source. Qualitatively, this twinning mechanism appears to be most prevalent. The second mechanism (*Twin 2*) involves glide of two leading partials along two different slip planes that intersect within a grain and the intersection point acts as the intragranular twin source. In line with experimental findings (Laplanche et al., 2017; Li et al., 2022; Praveen et al., 2018; Slone et al., 2018), most of the twins observed in the current study are nano-twins, as also reflected by the similar amount of strain accommodation in twin boundaries and twinned regions (Fig. 2b).

The energy barrier for nucleation of a twinning partial is controlled in part, by the unstable twin fault energy (γ_{ut}). Tadmor and Hai (2003) developed a criterion for calculating the twinning propensity as the ratio of the critical stress intensity factors (based upon Rice's formulation (Rice, 1992)). Once a leading partial dislocation has been emitted at a crack-tip, the ratio represents the competition between the nucleation of the trailing partial causing a perfect dislocation or the nucleation of another leading partial dislocation on an adjacent slip plane forming a nano-twin. Tadmor and Bernstein (2004) extended this criterion and introduced a twinnability parameter, ζ, defined as the twinning propensity normalized over all possible orientations of crack tips and slip systems in an FCC system. An approximate analytical expression of τ only depends on the ratios of different fault energies, i.e.,

$$\zeta = \left(1.136 - 0.151\frac{\gamma_{sf}}{\gamma_{us}}\right)\sqrt{\frac{\gamma_{us}}{\gamma_{ut}}} \tag{3}$$

According to this formulation, twinning is favored over perfect dislocation slip when $\zeta > 1$, which is more likely for smaller $\frac{\gamma_{sf}}{\gamma_{us}}$ and larger $\frac{\gamma_{us}}{\gamma_{ut}}$. It is important to note that the propensity of a mechanism to operate is defined here by the critical stress required for its nucleation, which should translate to a number of such events. However, each unit mechanism can have varying degrees of loading strain accommodation and/or number of participating atoms. Therefore, any comparison between predictions from this formulation (Eq. (3)) and simulation/experimental findings should be done carefully. While some studies directly compute/measure critical nucleation stress (Tadmor and Hai, 2003), others have used the amount of defect structure related to a mechanism, as a measure of its tendency (Tadmor and Bernstein, 2004; Zhang et al., 2017). In this study, we make comparisons based upon both percentage of total strain accommodated in loading direction (p_j) and fraction of total atoms (f_j) participating in twinning and perfect slip mechanisms.

Fig. 8a shows the ratios of contributions of twinning to perfect dislocation slip, as a function of the applied strain, during the later stages of loading for the NC MEA and Ni structures. Here, the contributions are calculated both in terms of percent total strain accommodation, i.e., $\frac{p_{twinning}}{p_{perfect\ slip}}$, and fraction of participating atoms, i.e., $\frac{f_{twinning}}{f_{perfect\ slip}}$. It can be observed that $\frac{p_{twinning}}{p_{perfect\ slip}} \cong 1$ and $\frac{p_{twinning}}{p_{perfect\ slip}} < \frac{f_{twinning}}{f_{perfect\ slip}}$ for the MEA structure with SRO. For MEA without SRO and Ni structure, $\frac{p_{twinning}}{p_{perfect\ slip}} < 1$, and $\frac{p_{twinning}}{p_{perfect\ slip}} \cong \frac{f_{twinning}}{f_{perfect\ slip}}$. It implies that the amount of strain accommodated per atom in perfect slip and twinning mechanisms are not identical in the MEA structure with SRO, in contrast

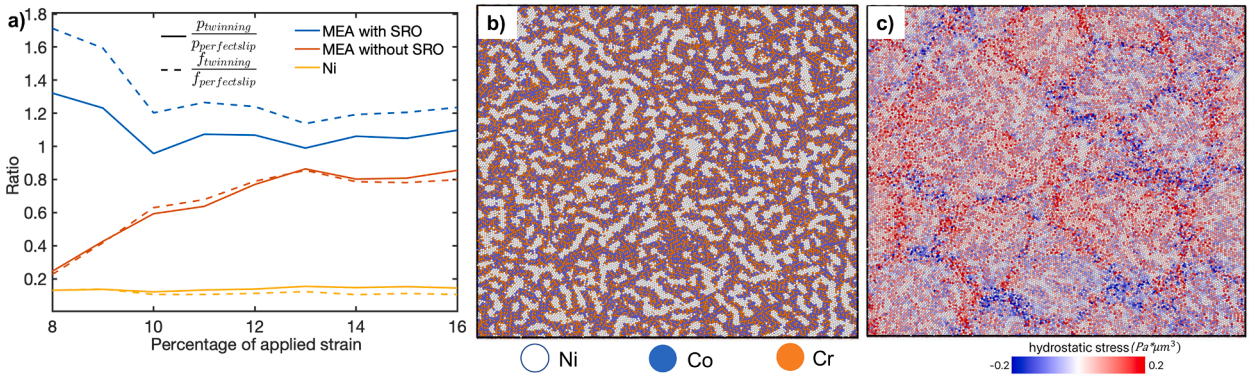

Fig. 8. (a) Ratios of contributions of twinning mechanism to perfect dislocation slip mechanism, calculated in terms of percent total strain accommodation $\frac{p_{twinning}}{p_{perfect\ slip}}$, and fraction of participating atoms $\frac{f_{twinning}}{f_{perfect\ slip}}$, plotted as function of applied strain during the uniaxial tensile testing of the 12 nm grain size NC structures of MEA with and without SRO, and Ni. Slices through deformed NC MEA structure of 12 nm grain size with SRO at 10% applied strain, colored according to **(b)** atom type and **(c)** atomic hydrostatic stress.

with the MEA structure without SRO and the Ni structure. The total strain accommodation per unit mechanism may vary further depending on the number of atoms comprised within a unit.

With the above caveats in place, we now compare the MD simulation results of the relative contributions of twinning mechanism to perfect dislocation slip (Fig. 8a) with the respective twinning propensities calculated from ζ (Table 3) for different NC structures. $\zeta = 0.96$ for pure Ni, which indicates that the critical stress is only slightly smaller for perfect slip than twinning, however, the atomistic simulations reveal almost no twinning in NC Ni structure in line with experimental observations (Frøseth et al., 2004). The relative contribution of twinning increases with applied strain in the MEA structure without SRO (Fig. 8a); however, it still remains smaller than the contribution of perfect dislocation slip at the end of loading, in contrast with the value of ζ (i.e., greater than 1). Thus, it can be said that the analytical formulation over-predicts the twinning contribution for these NC structures. This is plausible because the analytical formulation is derived for the crack tips where twins can easily nucleate due to stresses intensities, however, in NC structures, GBs often act as the twinning nucleation sites.

Twinning can be pronounced in NC structures wherein local GB structures can produce stress intensities (van Swygenhoven et al., 2003). It can be the case with MEA structure with SRO, where the value of ζ and the ratio of total strain accommodated in twinning to perfect dislocation slip mechanisms, are in agreement and close to one. In presence of SRO, the stress is more localized within the CoCr clusters as Ni-rich regions (Fig. 8b) correspond with the areas of zero hydrostatic stress (Fig. 8c), calculated as the first invariant of atomic stress tensor. The stress localization within these CoCr clusters that are also found to act as the preferred partial nucleation sites, can make twinning more pronounced and comparable with perfect dislocation slip.

Moreover, GPFE calculations only indicate the tendency of formation of a single defect, however, interactions between multiple defects in presence of SRO increases resistance to dislocation propagation, which is also suggested to promote twinning (Jian et al., 2020; Xie et al., 2022; Yang et al., 2022). Regardless of SRO, the relative contribution of twinning is more substantial in CoCrNi MEA structures, in contrast to pure Ni. Moreover, as seen in Fig. 2b, a cross-over between the combined mechanistic contributions of perfect dislocation slip and twinning, and the partial dislocation slip can be expected at values of applied strain above 16% in NC MEA structures. Thus, twinning and perfect dislocation slip can become dominant mechanisms in terms of microstructural strain accommodation during large deformation. This could explain the high ductility of MEA alloys.

4.4. Comparison with experiments

In experimental studies involving CoCrNi MEA, it is reported that deformation initially occurs by partial dislocations (Ding et al., 2019; Laplanche et al., 2017; Miao et al., 2017; Naeem et al., 2020; Slone et al., 2018; Uzer et al., 2018; Zhao et al., 2017). This experimental finding agrees well with our simulation results. The current study shows that together twinning and perfect dislocation glide should become the dominant IG mechanism on continued loading (i.e., >16% applied strain). In most experimental studies, twinning is listed as the dominant deformation mode during later stages of loading (Ding et al., 2019; Laplanche et al., 2017; Li et al., 2022; Miao et al., 2017; Naeem et al., 2020; Uzer et al., 2018; Zhao et al., 2017). But this comparison is often made against partial slip based on number of stacking faults and twin boundaries observed in the deformed microstructure.

In some experimental studies, it is stated that large deformation results in high dislocation densities; and their organization is attributed to the observation of dislocation cell structures in highly deformed CoCrNi MEA (Gao et al., 2022; Gludovatz et al., 2016;

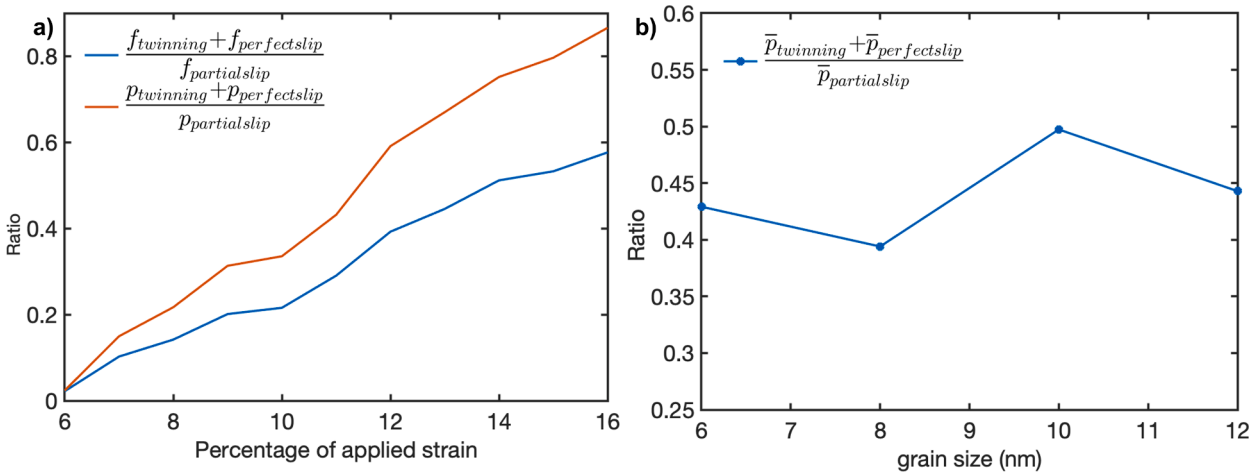

Fig. 9. **(a)** Ratios of contributions of perfect slip and twinning mechanisms combined to partial slip mechanism, calculated in terms of percent total strain accommodation $\frac{p_{twinning}+p_{perfect\ slip}}{p_{partial\ slip}}$, and fraction of participating atoms $\frac{f_{twinning}+f_{perfect\ slip}}{f_{partial\ slip}}$, as function of applied strain during the 10^8 s^{-1} uniaxial tensile testing of NC MEA structure with SRO and 12 nm grain size (**b**) Ratio of averages of percent total strain accommodation in the twinning and perfect slip mechanisms combined to partial slip mechanism during the flow regime $\frac{\overline{p}_{twinning}+\overline{p}_{perfect\ slip}}{\overline{p}_{partial\ slip}}$, as function of average grain size of the NC MEA structure with SRO.

Laplanche et al., 2017; Uzer et al., 2018). This could indicate pronounced perfect dislocation slip activity as well during later stages of deformation; however, the densities of dislocations and twins are not directly compared in these studies. Therefore, further experimental investigations are needed to validate the current simulation finding that both perfect dislocation slip, and twinning are the governing deformation mechanisms in CoCrNi MEA at larger values of applied strain.

As mentioned earlier, a comparison of the number/area/volume density of defect structures to assess the contribution of corresponding deformation mechanism might be misleading. For example, the ratios of contribution of perfect slip and twinning mechanisms to partial slip mechanism, calculated both in terms of percent total strain accommodation $\frac{p_{twinning} + p_{perfect\ slip}}{p_{partial\ slip}}$, and fraction of participating atoms $\frac{f_{twinning} + f_{perfect\ slip}}{f_{partial\ slip}}$, are shown in Fig. 9a for the MEA structure with SRO. The ratio calculated in terms of percent total strain accommodation is higher. It is because that both perfect dislocation slip and twinning mechanisms accommodate more strain per atom as compared to partial slip (Fig. 3). Moreover, even the same type of defect structure can have different strain accommodation due to the operation of multiple instances of a deformation mechanism. For example, two kinds of twins, and slipped regions by perfect dislocations can be seen in the deformed structure (Fig. 3) that exhibit different von Mises strain.

Lastly, any extrapolation between the simulation and the experimental findings must be performed with extreme caution due to several factors. One major consideration is the strain rate employed in MD simulations, which is often several orders of magnitude higher than experiments. It is previously suggested that during the short timescales that can be reasonably accessed by MD simulations, observation of perfect dislocation slip or twinning can be difficult, especially when the energy barrier for the nucleation of trailing partial or twin is large (Van Swygenhoven et al., 2004). However, this energy barrier can be overcome through GB relaxations or thermal fluctuations if the strain is increased slowly, as typically happens in experiments. Therefore, observation of large partial dislocation activity in MD simulation might be an artifact of the extremely fast loading rate.

In the current study, it is observed that the ratio of strain accommodation in the twinning and perfect slip mechanisms combined to the partial slip mechanism $\frac{p_{twinning} + p_{perfect\ slip}}{p_{partial\ slip}}$, at the end of loading of the 12 nm grain size MEA CoCrNi structure, decreases from 0.87 to 0.78, when the strain rate is increased from $10^8\ s^{-1}$ to $5 \times 10^8\ s^{-1}$. It indicates an increase in the contribution of partial slip to overall deformation when the strain rate is increased. Thus, it can be expected that on decreasing the strain rate to experimental values (i.e., of the order of 0.1–10 s^{-1}), the contribution of partial slip decreases; and the perfect slip and twinning can be the dominant mechanisms at smaller values of applied strain. While a direct quantification of this cross-over strain eludes experimental studies, it can be roughly estimated from the strain value at which the strain hardening rate changes. This is reported to be between 8 and 10% in experimental studies (Miao et al., 2017; Naeem et al., 2020; Slone et al., 2018), smaller than the value found from the extrapolation of Fig. 2b. in the current study. The ratio of strain accommodation in the twinning to perfect slip mechanism $\frac{p_{twinning}}{p_{perfect\ slip}}$, at the end of loading, is found to increase from 1.09 to 1.19 on increasing the strain rate, which suggests a rise in twinning propensity with strain rate. Recent experimental studies employing tensile tests over a wide range of strain rates (i.e., 10^{-3} to $10^3\ s^{-1}$), have confirmed this trend as well, where higher strain rate was reported to promote deformation twinning in CoCrNi MEA (Gao et al., 2022).

The other major difference between the simulation and experimental studies is the grain size regime surveyed. High density of twins, stacking faults, and dislocations are also reported in some experimental studies on NC CoCrNi MEA with 50 nm grain size (Praveen et al., 2018). In the current simulation study, the contribution of GB mechanisms decreases as the grain size is increased from 6 nm, with the IG mechanisms being the dominant deformation mechanism above 8 and 10 nm grain sizes in MEA structures with and without SRO, respectively (Fig. 4a). In the coarse-grained regime, the contribution of GB mechanisms can be expected to be minimal; with the operation of IG sources, such as Frank-Read, responsible for nucleation of dislocations and twins as compared to NC GBs (Spearot et al., 2019), which could further influence the relative contributions of IG mechanisms. Here, we don't find a steady trend in the variation of the ratio of percentages of total strain accommodation in the twinning and perfect slip mechanisms combined to partial slip mechanism $\frac{\bar{p}_{twinning} + \bar{p}_{perfect\ slip}}{\bar{p}_{partial\ slip}}$, when the grain size is decreased from 12 nm to 6 nm (Fig. 9b).

5. Conclusions

In this work, the deformation behavior of NC CoCrNi MEA alloys under uniaxial tension is investigated using large-scale MD simulations. The contributions of underlying deformation mechanisms towards overall strain accommodation are quantified using post-processing kinematic metrics and explained using estimates of planar fault energies. Specifically, the variations in the mechanistic contributions with grain size and SRO are studied. In summary, this research has shown the following:

- The contribution of partial dislocation slip is found to be the highest amongst all IG deformation mechanisms based upon the amount of strain accommodation. The contribution peaks around 10% applied strain and tends to decrease afterwards, which suggests that partial slip is the dominant IG mechanism during the initial loading in agreement with experimental findings. The large partial slip activity is attributed to small $\frac{\gamma_{sf}}{\gamma_{us}}$ ratio, whose value is found to decrease further with decreasing SRO.
- The trends in the variation of mechanistic contributions with applied strain indicate that the combined contribution of perfect dislocation slip and twinning mechanisms towards strain accommodation should become larger than the contribution of partial dislocation slip at larger values of applied strain. This result is in partial agreement with the experimental observation, where twinning is listed as the dominant deformation mode during later stages of loading, however, its contribution is not directly compared with perfect dislocation slip in such experimental studies.

- CoCrNi MEAs are found to have a larger $\frac{\gamma_{us}}{\gamma_{ut}}$ ratio and a smaller $\frac{\gamma_{sf}}{\gamma_{us}}$ ratio than pure Ni and thus, a higher twinning propensity; a trend also reflected in the relative contributions of deformation mechanisms from MD simulations. However, MD simulation results further suggest twinning to be more pronounced in the MEA structures with SRO than the ones without.
- The grain size that exhibits maximum flow stress is found to be smaller in NC MEA structures with SRO than the ones without. This finding suggests that in addition to increasing the strength, SRO delays the inverse Hall-Petch effect by lowering the contributions of GB mechanisms (e.g., sliding, atomic shuffling, etc.) across all grain sizes. Consequently, the strongest grain size below which GBs are found to govern the overall deformation, decreases in presence of SRO. It also verifies an important notion that the maximum strength of NC metals/alloys corresponds to a grain size where dominant deformation mechanism transitions from IG to GB based mechanisms.

Author contributions

AG, IJB and GJT conceived the project. AG performed simulations and subsequent calculations and prepared the first draft with inputs from all authors. WJ, SX, IJB and GJT revised the manuscript and added to the scientific discussion throughout its preparation.

Declaration of Competing Interest

Authors declare no competing financial interests.

Data availability

Data will be made available on request.

Acknowledgments

All authors are grateful for the support of the Office of Naval Research, Award Number: N00014-20-1-2788. AG and GJT also acknowledge the support of high-performance computing resources: Mio at CSM, and RMACC's Summit for performing simulations reported in this study.

Supplementary materials

Supplementary material associated with this article can be found, in the online version, at doi:10.1016/j.ijplas.2022.103442.

References

Cowley, J.M., 1950. An approximate theory of order in alloys. Phys. Rev. 77, 669–675. https://doi.org/10.1103/PhysRev.77.669.

Deng, H.W., Wang, M.M., Xie, Z.M., Zhang, T., Wang, X.P., Fang, Q.F., Xiong, Y., 2021. Enhancement of strength and ductility in non-equiatomic CoCrNi medium-entropy alloy at room temperature via transformation-induced plasticity. Mater. Sci. Eng. A 804, 140516. https://doi.org/10.1016/j.msea.2020.140516.

Deng, H.W., Xie, Z.M., Zhao, B.L., Wang, Y.K., Wang, M.M., Yang, J.F., Zhang, T., Xiong, Y., Wang, X.P., Fang, Q.F., Liu, C.S., 2019. Tailoring mechanical properties of a CoCrNi medium-entropy alloy by controlling nanotwin-HCP lamellae and annealing twins. Mater. Sci. Eng. A 744, 241–246. https://doi.org/10.1016/j.msea.2018.11.143.

Ding, J., Asta, M., Ritchie, R.O., 2018a. Melts of CrCoNi-based high-entropy alloys: atomic diffusion and electronic/atomic structure from ab initio simulation. Appl. Phys. Lett. 113 https://doi.org/10.1063/1.5045216.

Ding, J., Yu, Q., Asta, M., Ritchie, R.O., 2018b. Tunable stacking fault energies by tailoring local chemical order in CrCoNi medium-entropy alloys. Proc. Natl. Acad. Sci. USA. 115, 8919–8924. https://doi.org/10.1073/pnas.1808660115.

Ding, Q., Fu, X., Chen, D., Bei, H., Gludovatz, B., Li, J., Zhang, Z., George, E.P., Yu, Q., Zhu, T., Ritchie, R.O., 2019. Real-time nanoscale observation of deformation mechanisms in CrCoNi-based medium- to high-entropy alloys at cryogenic temperatures. Mater. Today 25, 21–27. https://doi.org/10.1016/j.mattod.2019.03.001.

El-Atwani, O., Li, N., Li, M., Devaraj, A., Baldwin, J.K.S., Schneider, M.M., Sobieraj, D., Wróbel, J.S., Nguyen-Manh, D., Maloy, S.A., Martinez, E., 2019. Outstanding radiation resistance of tungsten-based high-entropy alloys. Sci. Adv. 5, 1–10. https://doi.org/10.1126/sciadv.aav2002.

Feng, X., Surjadi, J.U., Fan, R., Li, X., Zhou, W., Zhao, S., Lu, Y., 2021. Microalloyed medium-entropy alloy (MEA) composite nanolattices with ultrahigh toughness and cyclability. Mater. Today 42, 10–16. https://doi.org/10.1016/j.mattod.2020.10.003.

Feng, X., Yang, H., Fan, R., Zhang, W., Meng, F., Gan, B., Lu, Y., 2020. Heavily twinned CoCrNi medium-entropy alloy with superior strength and crack resistance. Mater. Sci. Eng. A 788, 139591. https://doi.org/10.1016/j.msea.2020.139591.

Frøseth, A., Van Swygenhoven, H., Derlet, P.M., 2004. The influence of twins on the mechanical properties of nc-Al. Acta Mater. 52, 2259–2268. https://doi.org/10.1016/j.actamat.2004.01.017.

Gao, P., Ma, Z., Gu, J., Ni, S., Suo, T., Li, Y., Song, M., Mai, Y.W., Liao, X., 2022. Exceptional high-strain-rate tensile mechanical properties in a CrCoNi medium-entropy alloy. Sci. Chin. Mater. 65, 811–819. https://doi.org/10.1007/s40843-021-1798-6.

Garcia Filho, F.D.C., Ritchie, R.O., Meyers, M.A., Monteiro, S.N., 2022. Cantor-derived medium-entropy alloys: bridging the gap between traditional metallic and high-entropy alloys. J. Mater. Res. Technol. 17, 1868–1895. https://doi.org/10.1016/j.jmrt.2022.01.118.

Gludovatz, B., Hohenwarter, A., Thurston, K.V.S., Bei, H., Wu, Z., George, E.P., Ritchie, R.O., 2016. Exceptional damage-tolerance of a medium-entropy alloy CrCoNi at cryogenic temperatures. Nat. Commun. 7, 1–8. https://doi.org/10.1038/ncomms10602.

Gruber, J., Lim, H., Abdeljawad, F., Foiles, S., Tucker, G.J., 2017. Development of physically based atomistic microstructures: the effect on the mechanical response of polycrystals. Comput. Mater. Sci. 128, 29–36. https://doi.org/10.1016/J.COMMATSCI.2016.07.011.

Gupta, A., Gruber, J., Rajaram, S.S., Thompson, G.B., McDowell, D.L., Tucker, G.J., 2020a. On the mechanistic origins of maximum strength in nanocrystalline metals. npj Comput. Mater. 6, 153. https://doi.org/10.1038/s41524-020-00425-0.
Gupta, A., Rajaram, S.S., Thompson, G.B., Tucker, G.J., 2021. Improved computational method to generate properly equilibrated atomistic microstructures. MethodsX 8, 101217. https://doi.org/10.1016/j.mex.2021.101217.
Gupta, A., Zhou, X., Thompson, G.B., Tucker, G.J., 2020b. Role of grain boundary character and its evolution on interfacial solute segregation behavior in nanocrystalline Ni-P. Acta Mater. https://doi.org/10.1016/J.ACTAMAT.2020.03.012.
Han, B., Zhang, C., Feng, K., Li, Z., Zhang, X., Shen, Y., Wang, X., Kokawa, H., Li, R., Wang, Z., Chu, P.K., 2021. Additively manufactured high strength and ductility CrCoNi medium entropy alloy with hierarchical microstructure. Mater. Sci. Eng. A 820, 141545. https://doi.org/10.1016/j.msea.2021.141545.
He, H., Naeem, M., Zhang, F., Zhao, Y., Harjo, S., Kawasaki, T., Wang, B., Wu, X., Lan, S., Wu, Z., Yin, W., Wu, Y., Lu, Z., Kai, J.J., Liu, C.T., Wang, X.L., 2021. Stacking fault driven phase transformation in CrCoNi medium entropy alloy. Nano Lett. 21, 1419–1426. https://doi.org/10.1021/acs.nanolett.0c04244.
Hua, D., Xia, Q., Wang, W., Zhou, Q., Li, S., Qian, D., Shi, J., Wang, H., 2021. Atomistic insights into the deformation mechanism of a CoCrNi medium entropy alloy under nanoindentation. Int. J. Plast. 142, 102997 https://doi.org/10.1016/j.ijplas.2021.102997.
Inui, H., Kishida, K., Li, L., Manzoni, A.M., Haas, S., Glatzel, U., 2022. Uniaxial mechanical properties of face-centered cubic single- and multiphase high-entropy alloys. MRS Bull 47, 168–174. https://doi.org/10.1557/s43577-022-00280-y.
Jian, W.R., Wang, L., Bi, W., Xu, S., Beyerlein, I.J., 2021. Role of local chemical fluctuations in the melting of medium entropy alloy CoCrNi. Appl. Phys. Lett. 119, 121904 https://doi.org/10.1063/5.0064299.
Jian, W.R., Xie, Z., Xu, S., Su, Y., Yao, X., Beyerlein, I.J., 2020. Effects of lattice distortion and chemical short-range order on the mechanisms of deformation in medium entropy alloy CoCrNi. Acta Mater. 199, 352–369. https://doi.org/10.1016/j.actamat.2020.08.044.
Jian, W.R., Xie, Z., Xu, S., Yao, X., Beyerlein, I.J., 2022. Shock-induced amorphization in medium entropy alloy CoCrNi. Scr. Mater. 209, 114379 https://doi.org/10.1016/j.scriptamat.2021.114379.
Koch, C.C., 2017. Nanocrystalline high-entropy alloys. J. Mater. Res. 32, 3435–3444. https://doi.org/10.1557/jmr.2017.341.
Laplanche, G., Kostka, A., Reinhart, C., Hunfeld, J., Eggeler, G., George, E.P., 2017. Reasons for the superior mechanical properties of medium-entropy CrCoNi compared to high-entropy CrMnFeCoNi. Acta Mater. 128, 292–303. https://doi.org/10.1016/j.actamat.2017.02.036.
Li, J., Li, L., Jiang, C., Fang, Q., Liu, F., Liu, Y., Liaw, P.K., 2020a. Probing deformation mechanisms of gradient nanostructured CrCoNi medium entropy alloy. J. Mater. Sci. Technol. 57, 85–91. https://doi.org/10.1016/j.jmst.2020.03.064.
Li, L., Chen, H., Fang, Q., Li, J., Liu, F., Liu, Y., Liaw, P.K., 2020b. Effects of temperature and strain rate on plastic deformation mechanisms of nanocrystalline high-entropy alloys. Intermetallics 120. https://doi.org/10.1016/j.intermet.2020.106741.
Li, L., Chen, Z., Kuroiwa, S., Ito, M., Kishida, K., Inui, H., George, E.P., 2022. Tensile and compressive plastic deformation behavior of medium-entropy Cr-Co-Ni single crystals from cryogenic to elevated temperatures. Int. J. Plast. 148. https://doi.org/10.1016/j.ijplas.2021.103144.
Li, Q.J., Sheng, H., Ma, E., 2019. Strengthening in multi-principal element alloys with local-chemical-order roughened dislocation pathways. Nat. Commun. 10, 1–11. https://doi.org/10.1038/s41467-019-11464-7.
Miao, J., Slone, C.E., Smith, T.M., Niu, C., Bei, H., Ghazisaeidi, M., Pharr, G.M., Mills, M.J., 2017. The evolution of the deformation substructure in a Ni-Co-Cr equiatomic solid solution alloy. Acta Mater. 132, 35–48. https://doi.org/10.1016/j.actamat.2017.04.033.
Ming, K., Lu, W., Li, Z., Bi, X., Wang, J., 2020. Amorphous bands induced by low temperature tension in a non-equiatomic CrMnFeCoNi alloy. Acta Mater. 188, 354–365. https://doi.org/10.1016/j.actamat.2020.02.024.
Naeem, M., He, H., Zhang, F., Huang, H., Harjo, S., Kawasaki, T., Wang, B., Lan, S., Wu, Z., Wang, F., Wu, Y., Lu, Z., Zhang, Z., Liu, C.T., Wang, X.L., 2020. Cooperative deformation in high-entropy alloys at ultralow temperatures. Sci. Adv. 6 https://doi.org/10.1126/sciadv.aax4002.
Plimpton, S., 1995. Fast parallel algorithms for short-range molecular dynamics. J. Comput. Phys.
Praveen, S., Bae, J.W., Asghari-Rad, P., Park, J.M., Kim, H.S., 2018. Ultra-high tensile strength nanocrystalline CoCrNi equi-atomic medium entropy alloy processed by high-pressure torsion. Mater. Sci. Eng. A 735, 394–397. https://doi.org/10.1016/j.msea.2018.08.079.
Rajaram, S.S., Gupta, A., Thompson, G.B., Gruber, J., Jablokow, A., Tucker, G.J., 2020. Grain-size-dependent grain boundary deformation during yielding in nanocrystalline materials using atomistic simulations. Jom 72, 1745–1754. https://doi.org/10.1007/s11837-020-04036-4.
Rice, J.R., 1992. Dislocation nucleation from a crack tip: an analysis based on the Peierls concept. J. Mech. Phys. Solids 40, 239–271. https://doi.org/10.1016/S0022-5096(05)80012-2.
Sadigh, B., Erhart, P., Stukowski, A., Caro, A., Martinez, E., Zepeda-Ruiz, L., 2012. Scalable parallel Monte Carlo algorithm for atomistic simulations of precipitation in alloys. Phys. Rev. B Condens. Matter Mater. Phys. 85, 1–11. https://doi.org/10.1103/PhysRevB.85.184203.
Schuh, B., Völker, B., Todt, J., Kormout, K.S., Schell, N., Hohenwarter, A., 2018. Influence of annealing on microstructure and mechanical properties of a nanocrystalline CrCoNi medium-entropy alloy. Materials 11. https://doi.org/10.3390/ma11050662 (Basel).
Slone, C.E., Chakraborty, S., Miao, J., George, E.P., Mills, M.J., Niezgoda, S.R., 2018. Influence of deformation induced nanoscale twinning and FCC-HCP transformation on hardening and texture development in medium-entropy CrCoNi alloy. Acta Mater. 158, 38–52. https://doi.org/10.1016/j.actamat.2018.07.028.
Spearot, D.E., Tucker, G.J., Gupta, A., Thompson, G.B., 2019. Mechanical properties of stabilized nanocrystalline FCC metals. J. Appl. Phys. 126, 110901 https://doi.org/10.1063/1.5114706.
Stukowski, A., 2010. Visualization and analysis of atomistic simulation data with OVITO–the open visualization tool. Model. Simul. Mater. Sci. Eng. 18, 015012 https://doi.org/10.1088/0965-0393/18/1/015012.
Tadmor, E.B., Bernstein, N., 2004. A first-principles measure for the twinnability of FCC metals. J. Mech. Phys. Solids 52, 2507–2519. https://doi.org/10.1016/j.jmps.2004.05.002.
Tadmor, E.B., Hai, S., 2003. A Peierls criterion for the onset of deformation twinning at a crack tip. J. Mech. Phys. Solids 51, 765–793. https://doi.org/10.1016/S0022-5096(03)00005-X.
Tian, Y., Fang, Q., Li, J., 2020. Molecular dynamics simulations for nanoindentation response of nanotwinned FeNiCrCoCu high entropy alloy. Nanotechnology 31. https://doi.org/10.1088/1361-6528/ababcd.
Tucker, G.J., Foiles, S.M., 2015. Quantifying the influence of twin boundaries on the deformation of nanocrystalline copper using atomistic simulations. Int. J. Plast. 65, 191–205. https://doi.org/10.1016/J.IJPLAS.2014.09.006.
Tucker, G.J., Foley, D., Gruber, J., 2016. Continuum metrics for atomistic simulation analysis. Multiscale Materials Modeling for Nanomechanics.. In: Hull, Robert (Ed.), In: Springer Series in Materials Science, 245 Springer, Cham, pp. 297–315. https://doi.org/10.1007/978-3-319-33480-6_9.
Uzer, B., Picak, S., Liu, J., Jozaghi, T., Canadinc, D., Karaman, I., Chumlyakov, Y.I., Kireeva, I., 2018. On the mechanical response and microstructure evolution of NiCoCr single crystalline medium entropy alloys. Mater. Res. Lett. 6, 442–449. https://doi.org/10.1080/21663831.2018.1478331.
van Swygenhoven, H., Derlet, P.M., Budrovic, Z., Hasnaoui, A., 2003. Unconventional deformation mechanism in nanocrystalline metals? Int. J. Mater. Res. 94, 1106–1110. https://doi.org/10.1515/ijmr-2003-0201.
Van Swygenhoven, H., Derlet, P.M., Frøseth, A.G., 2004. Stacking fault energies and slip in nanocrystalline metals. Nat. Mater. 3, 399–403. https://doi.org/10.1038/nmat1136.
Van Swygenhoven, H., Derlet, P.M., Hasnaoui, A., 2002. Atomic mechanism for dislocation emission from nanosized grain boundaries. Phys. Rev. B 66, 24101. https://doi.org/10.1103/PhysRevB.66.024101.
Vo, N.Q., Averback, R.S., Bellon, P., Odunuga, S., Caro, A., 2008. Quantitative description of plastic deformation in nanocrystalline Cu: dislocation glide versus grain boundary sliding. Phys. Rev. B Condens. Matter Mater. Phys. 77, 134108 https://doi.org/10.1103/PhysRevB.77.134108.
Wang, J., Yang, H., Huang, H., Ruan, J., Ji, S., 2019a. Microstructure and mechanical properties of SiC whisker reinforced CoCrNi medium entropy alloys. Mater. Lett. 254, 77–80. https://doi.org/10.1016/j.matlet.2019.07.033.
Wang, J., Yang, H., Ruan, J., Wang, Y., Ji, S., 2019b. Microstructure and properties of CoCrNi medium-entropy alloy produced by gas atomization and spark plasma sintering. J. Mater. Res. 34, 2126–2136. https://doi.org/10.1557/jmr.2019.96.

Wang, W., Hua, D., Luo, D., Zhou, Q., Li, S., Shi, J., Wang, H., 2022. Molecular dynamics simulation of deformation mechanism of CoCrNi medium entropy alloy during nanoscratching. Comput. Mater. Sci. 203, 111085 https://doi.org/10.1016/j.commatsci.2021.111085.

Xie, Z., Jian, W.-R., Xu, S., Beyerlein, I.J., Zhang, X., Wang, Z., Yao, X., 2021. Role of local chemical fluctuations in the shock dynamics of medium entropy alloy CoCrNi. Acta Mater. 221, 117380 https://doi.org/10.1016/j.actamat.2021.117380.

Xie, Z., Jian, W., Xu, S., Beyerlein, I.J., 2022. Phase transition in medium entropy alloy CoCrNi under quasi-isentropic compression. Int. J. Plast. 157, 103389 https://doi.org/10.1016/j.ijplas.2022.103389.

Yang, X., Xi, Y., He, C., Chen, H., Zhang, X., Tu, S.T., 2022. Chemical short-range order strengthening mechanism in CoCrNi medium-entropy alloy under nanoindentation. Scr. Mater. 209, 114364 https://doi.org/10.1016/j.scriptamat.2021.114364.

Zhang, D.D., Zhang, J.Y., Kuang, J., Liu, G., Sun, J., 2021. Superior strength-ductility synergy and strain hardenability of Al/Ta co-doped NiCoCr twinned medium entropy alloy for cryogenic applications. Acta Mater. 220, 117288 https://doi.org/10.1016/j.actamat.2021.117288.

Zhang, R., Zhao, S., Ding, J., Chong, Y., Jia, T., Ophus, C., Asta, M., Ritchie, R.O., Minor, A.M., 2020a. Short-range order and its impact on the CrCoNi medium-entropy alloy. Nature 581, 283–287. https://doi.org/10.1038/s41586-020-2275-z.

Zhang, T.W., Ma, S.G., Zhao, D., Wu, Y.C., Zhang, Y., Wang, Z.H., Qiao, J.W., 2020b. Simultaneous enhancement of strength and ductility in a NiCoCrFe high-entropy alloy upon dynamic tension: micromechanism and constitutive modeling. Int. J. Plast. 124, 226–246. https://doi.org/10.1016/j.ijplas.2019.08.013.

Zhang, Zijiao, Sheng, H., Wang, Z., Gludovatz, B., Zhang, Ze, George, E.P., Yu, Q., Mao, S.X., Ritchie, R.O., 2017. Dislocation mechanisms and 3D twin architectures generate exceptional strength-ductility-toughness combination in CrCoNi medium-entropy alloy. Nat. Commun. 8 https://doi.org/10.1038/ncomms14390.

Zhao, S., Li, Z., Zhu, C., Yang, W., Zhang, Z., Armstrong, D.E.J., Grant, P.S., Ritchie, R.O., Meyers, M.A., 2021. Amorphization in extreme deformation of the CrMnFeCoNi high-entropy alloy. Sci. Adv. 7, 1–7. https://doi.org/10.1126/SCIADV.ABB3108.

Zhao, Y.L., Yang, T., Tong, Y., Wang, J., Luan, J.H., Jiao, Z.B., Chen, D., Yang, Y., Hu, A., Liu, C.T., Kai, J.J., 2017. Heterogeneous precipitation behavior and stacking-fault-mediated deformation in a CoCrNi-based medium-entropy alloy. Acta Mater. 138, 72–82. https://doi.org/10.1016/j.actamat.2017.07.029.

Zhou, L., Wang, Q., Wang, J., Chen, X., Jiang, P., Zhou, H., Yuan, F., Wu, X., Cheng, Z., Ma, E., 2022. Atomic-scale evidence of chemical short-range order in CrCoNi medium-entropy alloy. Acta Mater. 224, 16–18. https://doi.org/10.1016/j.actamat.2021.117490.

Zhou, X., Gupta, A., Tucker, G.J., Thompson, G.B., 2021. Manipulation of solute partitioning mechanisms for nanocrystalline stability. Acta Mater., 116662 https://doi.org/10.1016/j.actamat.2021.116662.

Zimmerman, J.A., Bammann, D.J., Gao, H., 2009. Deformation gradients for continuum mechanical analysis of atomistic simulations. Int. J. Solids Struct. 46, 238–253. https://doi.org/10.1016/j.ijsolstr.2008.08.036.